State of residual stress in laser-deposited ceramic composite coatings on aluminum alloys

Kadolkar, P. B.; Watkins, T. R.; De Hosson, J. Th. M.; Kooi, B. J.; Dahotre, N. B.

Published in:
Acta Materialia

DOI:
10.1016/j.actamat.2006.07.049

Publication date:
2007

Available online at www.sciencedirect.com
ScienceDirect
Acta Materialia 55 (2007) 1203–1214
Acta MATERIALIA
www.actamat-journals.com

State of residual stress in laser-deposited ceramic composite coatings on aluminum alloys

P.B. Kadolkar [a], T.R. Watkins [b], J.Th.M. De Hosson [c], B.J. Kooi [c], N.B. Dahotre [a,*]

[a] *Department of Materials Science and Engineering, Center for Laser Applications, University of Tennessee, 1512 Middleway, 326 Dougherty Engineering Building, Knoxville, TN 37996, USA*
[b] *High Temperature Materials Laboratory, Materials Science and Technology Division, Oak Ridge National Laboratory, Oak Ridge, TN 37831, USA*
[c] *Department of Applied Physics, Materials Science Center and The Netherlands Institute of Metals Research, University of Groningen, Nijenborgh 4, 9747 AG, Groningen, The Netherlands*

Received 24 January 2006; received in revised form 11 July 2006; accepted 12 July 2006
Available online 6 December 2006

Abstract

The nature and magnitude of the residual stresses within laser-deposited titanium carbide (TiC) coatings on 2024 and 6061 aluminum (Al) alloys were investigated. Macro- and micro-stresses within the coatings were determined using an X-ray diffraction method. Owing to increased debonding between the coating and the substrate, the macro-stresses were found to be compressive and to decrease in magnitude with increasing processing speed. The origin of the macro- and micro-stresses is discussed. To that end, transmission electron microscopy observations showed no evidence of plastic deformation within selected coatings. The micro-stresses in the TiC particulate and aluminum matrix phases within the coatings were found to be independent of the amount of debonding. This study could assist in optimizing the processing parameters to fabricate composite coatings for specific applications.

Keywords: Residual stresses; Laser treatment; Composites; Coatings; X-ray diffraction

1. Introduction

Ceramic composite coatings produced by lasers have been envisioned as protective coatings for several technological applications such as hard coatings for cutting tools, corrosion- and erosion-resistant coatings for die casting dies, wear-resistant coatings for engine bores, and protective coatings for advanced power engineering applications [1–3]. The functionality and reliability of these composite coatings largely depend on the residual stresses developed during fabrication of the coatings. Residual stresses in composite coatings develop as a result of differences in mechanical and thermal properties of the different phases (matrix and reinforcement) or layers of materials (coating and substrate). The presence of residual stresses can prove either detrimental or beneficial to performance. The state of residual stress can have a significant influence on the yield strength and fatigue strength of composite coatings. Generally, in a metallurgically/chemically bonded coating, compressive stresses in the coating are considered more favorable than the tensile stresses, because they increase the fatigue life of the component. However, extremely high stresses can lead to delamination, intra-coating fracture and yielding or cracking of the coating and, in general, can undermine the performance of the component [4]. Therefore, knowledge of the residual stress state and its variation with processing conditions is necessary in order to achieve coatings optimized for practical applications.

In the present investigation, laser-deposited TiC/Al composite coatings on two aluminum alloy substrates, namely 2024 and 6061, were prepared using laser traverse speeds of 150, 175 and 200 cm/min and 100, 125 and

* Corresponding author. Tel.: +1 865 974 3609.
E-mail address: ndahotre@utk.edu (N.B. Dahotre).

1359-6454/$30.00
doi:10.1016/j.actamat.2006.07.049

150 cm/min, respectively. Residual stresses and debonding were characterized within the coated samples using X-ray diffraction and scanning electron microscopy (SEM) techniques, respectively.

2. Theory and background

2.1. Origin of residual stresses in composite coating

Residual stresses are defined as 'self-equilibrating internal stresses existing in a free body which has no external forces or constraints acting on its boundary' [5,6]. Often in a coating/substrate system, residual stresses arise owing to thermal expansion mismatch between the coating and the substrate when cooled from its fabrication temperature. Assuming no deformation of the substrate and assuming that the substrate reaches the same deposition temperature as the coating, the thermal stresses developed in a homogeneous coating can be derived as [4]:

$$\sigma_T = \frac{E_c E_s t_s (\alpha_c - \alpha_s)\Delta T}{(1-\nu)(E_s t_s + E_c t_c)} \quad (1)$$

where σ_T is the thermal residual stress in the coating, ΔT is the difference between the processing temperature and the stress measurement temperature (room temperature), α is the coefficient of thermal expansion, E is Young's modulus, t is the thickness and ν is Poisson's ratio. The subscripts c and s refer to the coating and substrate, respectively. Compressive coating stresses are developed when $\alpha_c < \alpha_s$, and tensile stresses are developed when $\alpha_c > \alpha_s$. It should be emphasized that Eq. (1) is for thermal residual stress and that the overall residual stress could include strains from other factors, such as deformation.

Residual stresses may be classified into three types: macro-stresses, micro-stresses and root mean square (RMS) stresses. Macro-stresses are often homogeneous, extending over macroscopic distances, and often arise during fabrication processes such as rolling, cutting, machining, joining, etc. They occur owing to volume/property differences of one region of the material relative to another. However, micro-stresses occur over microscopic volumes such as particles or grains and occur (a) owing to the differences in the thermal, elastic and plastic properties of the phases and/or grain orientations, and (b) owing to coherency strains at the matrix/reinforcement interface [7]. RMS stresses and strains occur over nanoscopic regions, sub-grains or crystallites and are typically determined from diffraction peak broadening or by micro-beam diffraction methods. The origins of these strains are given above, when they are not homogeneous within the diffracting volume.

2.2. Residual stresses in laser surface treatments

Laser surface treatment for forming composite coating consists of rastering a directed high-energy laser beam on a ceramic precursor layer that is pre/co-deposited on the metallic substrate. When the substrate melts, the ceramic and the substrate undergo convective mixing over a very short interaction time [8]. As the laser beam traverses forward, the molten pool cools rapidly (10^3–10^8 K/s) [9,1] to form a composite coating consisting of the particulate reinforcements uniformly distributed in the metal matrix. The convective behavior of the molten pool largely depends on the laser conditions such as the laser power density, the laser beam size, laser beam profile and the laser interaction time.

Residual stresses in laser surface treatments are primarily developed owing to the large temperature differences experienced by the surface relative to the bulk of the substrate during laser–material interaction. Earlier studies have shown that the average residual stresses developed in a metal or alloy surface treated either by a single or series of laser tracks are tensile, except for some steels where compressive stresses are developed owing to martensite formation [10–13]. The two major sources for residual stresses realized during laser surface treatments are plastic deformation during thermal expansion/contraction and volume changes due to local phase transformation. The development of stresses in single laser track in a single-phase alloy system can be explained sequentially. During heating, a thin layer of the substrate is melted. Upon cooling, the track will solidify, starting at the melt/substrate interface (both in the sides and the bottom of the laser track) by conducting heat to the substrate. Since the substrate behaves as a large thermal sink, the side and the bottom of the molten pool cools and contracts faster than the center. When the center solidifies, this difference in the contraction is compensated by plastic deformation of the center, which is at a higher temperature than the rest of the coating. When all is at room temperature, the resulting residual stresses are tensile [14]. In the case of some steels, where rapid solidification is associated with volume expansion owing to the austenite to martensite phase change, compressive stresses are generated in this last region of solidification [10,11].

In materials treated with multiple laser tracks, the stresses have been found to be similar to those in single tracks, except for an increase in the maximum value of tensile stresses in the previously laid tracks as successive adjacent tracks are deposited [15]. In situations where compressive stresses are developed owing to martensite formation, again each new overlapping laser track exerts tensile stresses and produces an annealing effect on the previous track, thus relieving the compressive stresses and putting the entire surface into tension [15].

2.3. Principle of X-ray stress determination in composite coating

The residual stresses can be determined using an X-ray diffraction method because it is non-destructive, surface localized, and phase distinctive [16–18]. In the X-ray diffraction technique, the crystal plane spacing is used as an absolute strain gauge for strain/stress measurement. The

interplanar spacing d for a particular set of *hkl* planes of a given phase can be determined from the peak position in the diffraction pattern, using Bragg's law. Comparing these interplanar spacings with the unstressed interplanar spacing allows calculation of the strain normal to the particular *hkl* planes. In order to get a reliable stress/strain determination, several measurements are made on the sample at different sample tilt angles ψ. The tilt angle ψ is the angle between the surface normal and the normal to the diffracting planes. The direction of strain measurement $\varepsilon_{\phi\psi}$ is within the plane defined by ψ and the azimuthal angle, ϕ (Fig. 1). Generally, when strain measurements are made using at least six independent directions defined by ϕ and ψ, all the components of the strain tensor for each phase can be obtained. From these strains, the corresponding stress components can be calculated using the elastic constants appropriate for the selected *hkl* plane [19].

In this particular stress study, the stresses were calculated using the Dölle–Hauk method [20], assuming a triaxial stress state. The fully expanded equation relating strain to stress is given as:

$$\begin{aligned}\varepsilon_{\phi\psi} &= \frac{(d_{\phi\psi}-d_0)}{d_0} \\ &= \frac{(1+\nu)}{E}\cdot\{\sigma_{11}\cos^2\phi+\sigma_{12}\sin 2\phi+\sigma_{22}\sin^2\phi-\sigma_{33}\} \\ &\quad\cdot\sin^2\psi+\frac{(1+\nu)}{E}\cdot\sigma_{33}-\frac{\nu}{E}\cdot(\sigma_{11}+\sigma_{22}+\sigma_{33}) \\ &\quad+\frac{(1+\nu)}{E}\cdot\{\sigma_{13}\cos\phi+\sigma_{23}\sin\phi\}\cdot\sin 2\psi \end{aligned} \quad (2)$$

where ε and d_0 are the strain and the stress-free interplanar spacing, respectively. The above equation consists of six unknowns, σ_{11}, σ_{12}, σ_{22}, σ_{33}, σ_{13}, σ_{23} and can be solved if $d_{\phi\psi}$ is measured along three directions when the relative ϕ orientations are 0°, 45° and 90° [6].

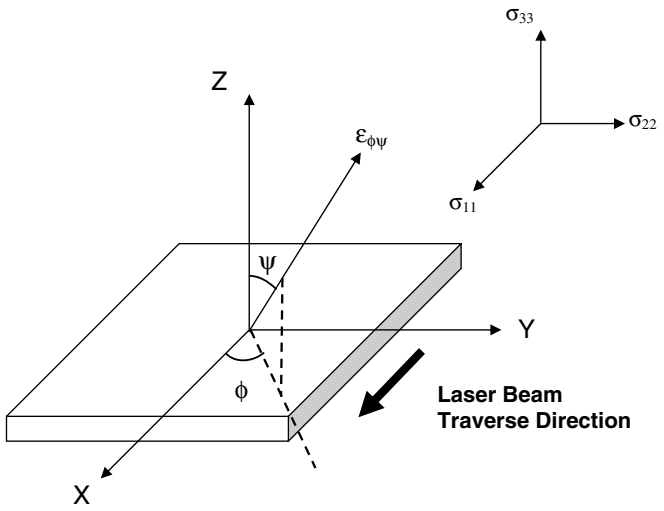

Fig. 1. Specimen coordinate system during X-ray stress measurement. Here, $\phi = 0$ is chosen to be the x direction, parallel to the laser tracks, and $\phi = 90$ is chosen to be the y direction, perpendicular to the laser tracks.

The results obtained from Eq. (2) represent the total stresses existing in each phase. Since the system is composite in nature, these total stresses may be further separated into macro-stresses and micro-stresses as follows. The macro-stress in a coating is assumed to be the same at each location. Each component of the total stress tensor in each phase (in the present case, the coating is a composite of Al and TiC) can then be written as the sum of the macro- and micro-contributions.

$$^{t}\sigma_{ij}^{Al} = {}^{m}\sigma_{ij} + {}^{\mu}\sigma_{ij}^{Al} \quad (3)$$

$$^{t}\sigma_{ij}^{TiC} = {}^{m}\sigma_{ij} + {}^{\mu}\sigma_{ij}^{TiC} \quad (4)$$

where superscripts, t, m and μ refer to total, macro and micro, respectively. Here, both contributions are assumed to be predominantly due to thermal residual stresses. The equation of equilibrium for the micro-stress components, based on the rule of mixture for the volume fraction of the components of coating, is given as [6]:

$$(1-f)^{\mu}\sigma_{ij}^{Al} + f^{\mu}\sigma_{ij}^{TiC} = 0 \quad (5)$$

where f is the volume fraction of TiC particles. Micro-stresses are likely to be inhomogeneous on both the macro- and microscopic scales [6]. The measurement of these stresses within individual grains may require probe sizes only available at specialized synchrotron sources. However, if the probe size is large enough, an average micro-stress can be determined. For this work, the micro-stresses in Eqs. (3)–(11) are considered to be average micro-stresses. It is assumed that the measurement volumes are large enough to provide the average micro-stresses that are constant and independent of measurement location. As discussed in Noyan and Cohen [6], bulk, surface force and moment balances are underlying assumptions as well. Solving Eqs. (3)–(5) for three unknowns gives ${}^{m}\sigma_{ij}$, ${}^{\mu}\sigma_{ij}^{Al}$, and ${}^{\mu}\sigma_{ij}^{TiC}$ in terms of the total stresses ${}^{t}\sigma_{ij}^{Al}$ and ${}^{t}\sigma_{ij}^{TiC}$:

$$^{\mu}\sigma_{ij}^{Al} = f\left({}^{t}\sigma_{ij}^{Al} - {}^{t}\sigma_{ij}^{TiC}\right) \quad (6)$$

$$^{\mu}\sigma_{ij}^{TiC} = (1-f)\left({}^{t}\sigma_{ij}^{TiC} - {}^{t}\sigma_{ij}^{Al}\right) \quad (7)$$

$$^{m}\sigma_{ij} = (1-f)^{t}\sigma_{ij}^{Al} + f^{t}\sigma_{ij}^{TiC} \quad (8)$$

The micro-stresses in each phase and the macro-stresses can thus be calculated from Eqs. (6)–(8) using the total stresses obtained from the X-ray stress measurements [19].

3. Experimental procedure

3.1. Material and coating process

Commercially available TiC powder supplied by CERAC Milwaukee, WI (99.5% purity, average powder size <15 μm) and Al alloys, 2024-T4 (nominally 3.8–4.9 wt.% Cu, 0.5 wt.% Si, 0.5 wt.% Fe, 0.3–0.9 wt.% Mn, 1.2–1.8 wt.% Mg, 0.10 wt.% Cr, balance Al) and 6061–T4

(0.8–1.2 wt.% Mg, 0.4–0.8 wt.% Si, 0.15–0.4 wt.% Cu, 0.04–0.35 wt.% Cr, 0.7 wt.% Fe, <0.15 wt.% Mn, balance Al), were used in the present study [21]. Blocks of 2024 and 6061 Al alloy with dimensions $75 \times 75 \times 25$ mm^3 were lightly cleaned using sand blasting. Then a precursor coating consisting of TiC powder (particle size of 20 ± 10 μm) suspended in a proprietary 10 wt.% water-based organic binder was spray deposited on both 2024 and 6061 Al substrates. The average precursor deposit thickness was 150 ± 10 μm. Based on prior experience, sprayed coupons were fully dried at 70 °C for 1 h for complete removal of moisture prior to laser processing.

A 2-kW Rofin Sinar continuous wave Nd:YAG laser equipped with a fiber optic beam delivery system (17 m long and core diameter 600 μm) was employed. The fiber optic beam delivery provided efficient (<5% loss) laser energy input to the workpiece. The laser beam was focused at 0.5 mm above the surface of the substrate. The lenses within the output-coupling module of fiber optic were configured to provide a line beam (3.5×0.6 mm^2) spatially onto the sample surface. To cover the entire surface area of the block, a series of laser tracks were made adjacent to each other with 20% overlap. The laser power was held constant at 2 kW, while the laser traverse speeds were varied. The laser scan speeds used for 2024 and 6061 Al alloy substrates were 150, 175 and 200 cm/min and 100, 125 and 150 cm/min, respectively, and were selected based upon previous research and substrate thermal conductivities [1]. As 6061 Al alloy has higher thermal conductivity (154 W/mK) compared with 2024 Al alloy (120 W/mK) [21], a set of lower scan speeds were explored in order to ensure enough 'interaction' time and sufficient heat for melting.

3.2. Microstructural characterization

Samples for microstructural characterization were sectioned perpendicular to the laser tracks from each block. The cross-sectional samples for metallographic studies were polished on a Buehler Isomet 2000 cloth to a diamond finish and etched with Kellers reagent to reveal the microstructure evolved during laser processing. Microstructural characterization was performed on a Hitachi S3500 Variable Pressure SEM instrument to observe the effects of the process variables on the particle distribution and the interface region between the coating and the substrate.

Samples for transmission electron microscopy (TEM) were prepared using spark cutting erosion first to retrieve plan-view sections from the coatings and then ion-milled to thin down the samples for electron transparence. High resolution microscopy of the samples was executed with a JEOL JEM2010-FEG operating at 200 kV.

3.3. X-ray measurements

The specimens used for X-ray stress measurement were cut from each block into $30 \times 30 \times 7$ mm^3 sections. The blocks were first cut on the high-speed grinding cutter to remove the excess substrate material from the bottom away from the coating. The water coolant was used to ensure that the heat from the high-speed grinding was not altering the material. This was followed by sectioning of the sample on the slow speed diamond saw in order to avoid introduction of any additional stresses in the coating during the cutting process. This method of sample preparation is not expected to change the stress state. The specimens were handled carefully in order to avoid any damage to the coated surface during sample preparation.

X-ray strain measurements were carried out at Oak Ridge National Laboratory using a PANalytical X'Pert Pro MPD Q-Q goniometer with parallel-beam optics and following experimental conditions: Cu Kα radiation from an X-ray tube operated at 45 kV, 40 mA; incident parabolic mirror; 0.09° radial divergence limiting slits and Xe proportional detector. The surface roughness of the specimens within each laser track was measured using a Perthometer M1 roughness measuring meter which read an average value of $R_a = 1.1$ μm. The average surface roughness of the specimens including the overlapping regions between adjacent laser tracks was measured to be $R_a = 40$ μm. The parallel beam method used in this study was primarily chosen to compensate for the surface roughness imposed by the overlapping regions during the X-ray strain measurement [22,23]. In addition to the specimen roughness, the parallel beam method also helps in minimizing the errors due to the specimen positioning, thus increasing the accuracy in the measured stress values [6,23,24]. Specimen alignment was accomplished using a dial gauge probe, which was accurate to ±5 μm.

The (420) reflection of Al at 116.6° 2θ and (422) reflection of TiC at 121.4° 2θ were selected for X-ray stress analysis. Accordingly, data were collected on the coated samples over the range of 114–124° 2θ using a 0.05° 2θ step interval and step times of 10 s step^{-1}. Generally, (*hkl*) reflection lines with Bragg angles $2\theta > 130°$ with sufficient intensity are selected to maximize the peak shift for a given strain and thus achieve high accuracy in peak position determination [7]. However, in this study, it was difficult to find an intense TiC peak in the high 2θ region with Cu Kα radiation, which did not overlap with a peak from Al. Hence the (420) reflection of Al and (422) reflection of TiC were selected as peaks with Bragg angles $2\theta > 105°$ and sufficient intensity values. Measurements were made at ϕ values of 0°, 45° and 90° and at ψ values of 0°, ±27.6°, ±41 and ±53.5°. The actual irradiated area on the specimen surface at ψ tilt angles of −53.5° and +53.5° were measured using a X-ray photographic film to be 20×30 mm^2 and 20×2 mm^2, respectively. To obtain the diffracted peak 2θ positions precisely, all the raw data profiles were fitted to a pseudo-Voigt function using a profile fitting software (Profit 1.0, Philips Analytical). Lorentz polarization, absorption and background corrections were also applied to the diffraction peak profiles. The maximum and the minimum penetration depths for the range of ψ tilt angles (for 99% of the diffracted signal) were calculated to

be ~48 μm and ~12 μm, respectively, and were effectively the same for both the substrates owing to the similar densities [6]. These penetration depths were found to be sufficiently larger than the size of the TiC particles (<12 μm) thus, ensuring that the stresses measured by this method were characteristic of the composite nature of the coating and represent average values over a considerable depth below the surface of the coating.

The stress-free TiC interplanar spacing was determined via a θ–2θ scan from a thin uniform layer of this powder, deposited as a slurry onto a flat silicon zero background plate. The peak obtained was then profile fit to get the exact 2θ position from which d_0 was calculated using Bragg's law. The stress-free interplanar spacing for Al in the composite was, however, calculated from the '$d_{\phi\psi}$ vs. $\sin^2\psi$' plots using the method given in reference [6] and assuming a biaxial stress state in the irradiated X-ray volume.

To obtain a representative standard deviation for the diffracted peak positions, scans at $\psi = 53.5°$ with $\phi = 0°$ were repeated 10 times on one of the specimens, using the same X-ray conditions as before, and the estimated standard deviation for this peak was calculated. Each time the sample was randomly shifted in the sample holder before repeating the run. This estimated standard deviation value was assumed to be the same for all ϕ and ψ values and the same over all the specimens processed under different laser traverse speeds. The variances in the calculated micro- and macro-stresses were obtained using the above-mentioned Eqs. (6)–(8), assuming uncorrelated errors, giving:

$$V\left({}^{\mu}\sigma_{ij}^{\mathrm{Al}}\right) = f^2\left[V\left({}^{t}\sigma_{ij}^{\mathrm{Al}}\right) + V\left({}^{t}\sigma_{ij}^{\mathrm{TiC}}\right)\right] \tag{9}$$

$$V\left({}^{\mu}\sigma_{ij}^{\mathrm{TiC}}\right) = (1-f)^2\left[V\left({}^{t}\sigma_{ij}^{\mathrm{Al}}\right) + V\left({}^{t}\sigma_{ij}^{\mathrm{TiC}}\right)\right] \tag{10}$$

$$V({}^{m}\sigma_{ij}) = (1-f)^2 V\left({}^{t}\sigma_{ij}^{\mathrm{Al}}\right) + f^2 V\left({}^{t}\sigma_{ij}^{\mathrm{TiC}}\right) \tag{11}$$

which were used to calculate the standard deviations within these stress values. Standard deviations are obtained in order to take into account both the effects of the non-homogeneity within the specimens and the uncertainties from the profile fitting [19].

4. Results and discussion

4.1. Microstructural characterization

Fig. 2 illustrates a typical cross-section of the coating produced by this technique. The coating is composite in nature, with TiC particles of various sizes uniformly distributed in the Al matrix. Quantitative analysis of the micrograph indicates that TiC particles occupy 60–65 vol.% in the coating. The variation in size distribution of the particles within the coating can be attributed to the variation in size of particles within the original powder mixture (20 ± 10 μm). Fig. 3(a)–(f) are the cross-sectional

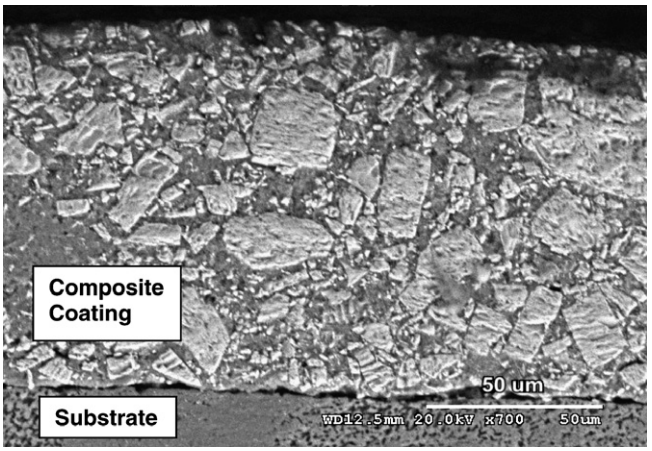

Fig. 2. SEM micrograph of coating showing uniform distribution of TiC particles within Al matrix.

views of the interface between the coating and the heat-affected region of the substrate for all the samples. At the lower laser traverse speeds (150 and 175 cm/min for 2024 Al and 100 cm/min for 6061 Al) the bond between the coating and the substrate is sound (Fig. 3a, b and d, respectively). However, at higher laser traverse speeds (200 cm/min for 2024 Al; and 125 and 150 cm/min for 6061 Al), the coating starts to debond (Fig. 3c, e and f, respectively). Those micrographs with interfacial cracks were taken at 'worst case' locations to show partial debonding. It was interesting to note that, at the highest traverse speed, especially in the case of 6061 Al alloy, the coatings in Fig. 3e and f were debonded at most of the locations along the interface with the substrate.

4.2. X-ray stress measurement and TEM

Diffraction patterns are shown in Fig. 4 for the 2024 Al substrate sample processed at 150 cm/min at seven ψ angles (0°, ±27.6°, ±41 and ±53.5°) at $\phi = 0°$. Careful examination of the spectra shows a shift in the 2θ positions as a function of ψ angle, which is considered to be due to residual stress. Similar measurements of peak position/interplanar spacing were performed at angles ϕ of 45° and 90°. This process of measurement of interplanar spacings for all ϕ and ψ angle positions was then repeated on all the samples processed under different parameters.

Comparison of the TiC and Al reflections indicate no abrupt changes in the relative intensities with tilt angle, suggesting the absence of any strong crystallographic texture or preferred orientation. Similar observations were also made in case of 6061 Al alloy substrates. Figs. 5a and 5b show the '$d_{\phi\psi}$ vs. $\sin^2\psi$' plots for Al (420) (matrix) and TiC (422) (reinforcement) reflections, respectively, obtained at different ϕ (0°, 45°, 90°) angles. Each of these plots shows a near linear variation of $d_{\phi\psi}$ obtained for $\psi > 0$ and $\psi < 0$ values. Similar trends were observed in the '$d_{\phi\psi}$ vs. $\sin^2\psi$' plots for Al and TiC phases from

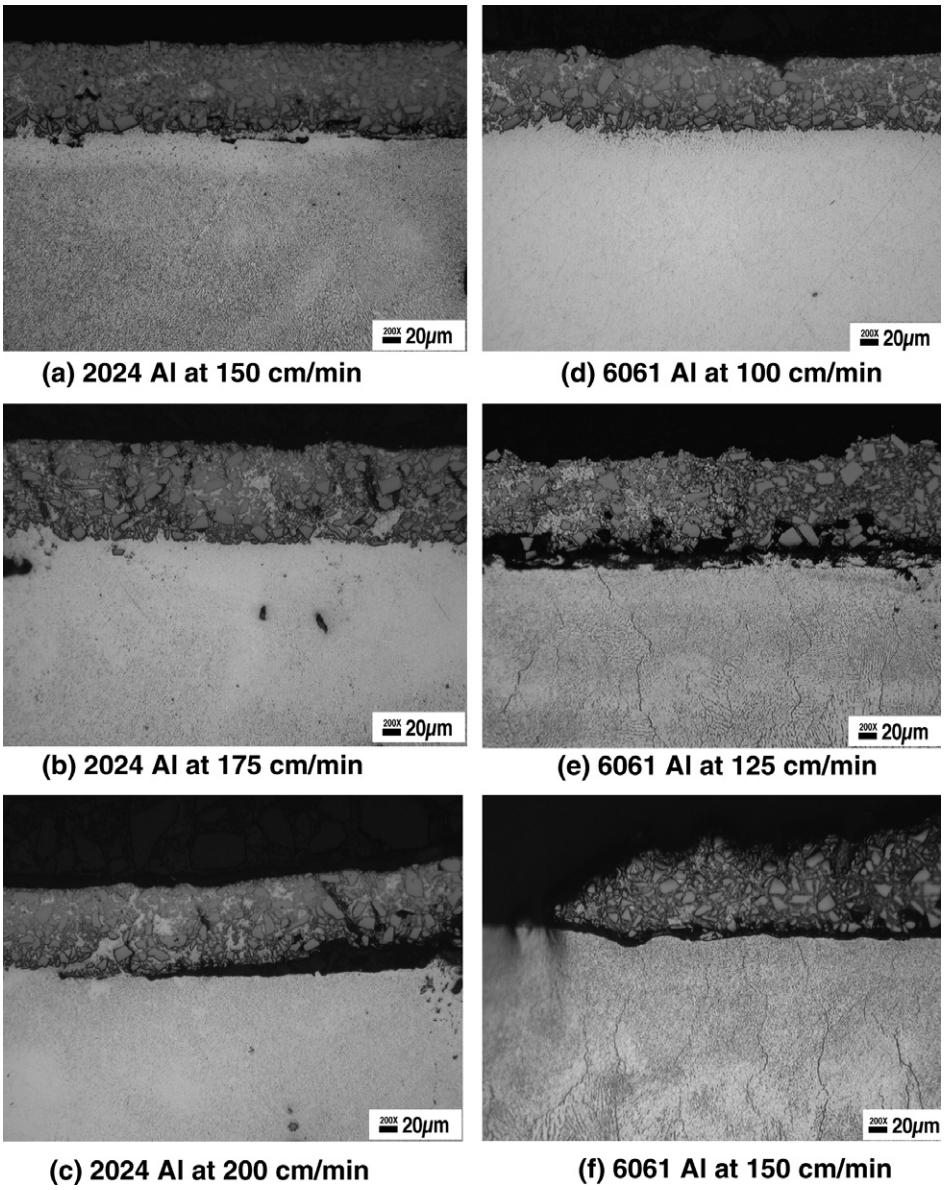

Fig. 3. SEM micrographs showing the cross section of the coatings processed at various speeds. (a) 2024 AI at 150 cm/min, (b) 2024 AI at 175 cm/min, (c) 2024 AI at 200 cm/min, (d) 6061 Al at 100 cm/min, (e) 6061 Al at 125 cm/min, (f) 6061 Al at 150 cm/min.

coatings on 6061 Al alloy [25]. Linear trends in Al (420) and TiC (422) reflections indicate negligible shear stresses and no significant plastic deformation within the X-ray penetration volume [5,26]. In an earlier effort by one of the authors, however, plastic deformation of the ceramic phase due to the existence of high-density defects in the form of closed space stacking faults was observed [27] within laser processed silicon carbide/aluminum composites. Such faults are due to extreme thermal conditions (rapid heating/cooling) and reflect the thermal and/or mechanical history of the phase.

The state of stress in the coating can be influenced by the microstructural features such as type and nature of phases and dislocations evolved during laser processing. Such features can be appropriately revealed and characterized employing TEM analysis. In the current work, an overview of the various phases in TiC/Al coating on 6061 and on 2024 Al alloy substrates processed at 100 and 150 cm/min, respectively, are presented in TEM micrographs in Fig. 6. In the former case (TiC/Al coating on 6061 processed at 100 cm/min) the precipitates in the matrix were Si, $TiSi_2$ and AlMgSiFe (Fig. 6a), and some $TiSi_2$ precipitates were attached to the TiC particles (Fig. 6b). This is in contrast to TiC/Al coating on 2024, where Al_2O_3, Al_2Cu and AlSiMnFe were found in the vicinity of the TiC particle (Fig. 6c), and $TiSi_2$ precipitates were present in the matrix away from the TiC particles. The phases were analyzed using EDS spectroscopy. Compounds such as AlMgSiFe, Al_2Cu and AlSiMnFe are phases inherent in the respective alloy systems, whereas $TiSi_2$ and Al_2O_3 are metastable phases existing owing to the non-equilibrium conditions prevailing during laser processing. As mentioned

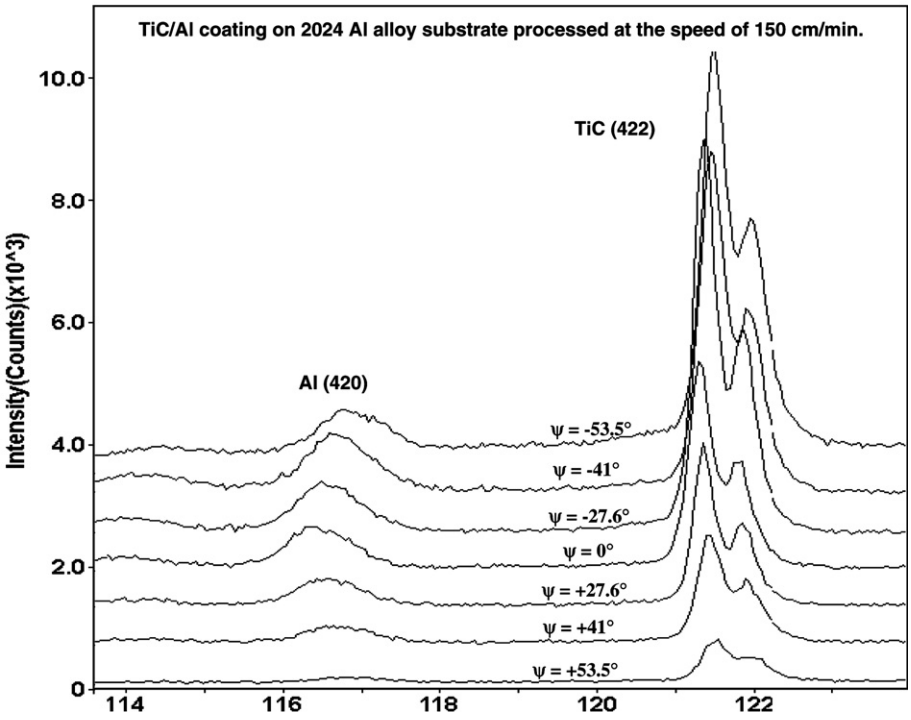

Fig. 4. Diffraction patterns showing change in the 2θ positions with change in ψ angle at $\phi = 0°$.

above, although plastic deformation of the phases/precipitates (Si, TiC, $TiSi_2$, Al_2O_3, Al_2Cu, AlMgSiFe and AlSiMnFe) and the matrix (aluminum) around them was expected, no dislocation structures or stacking fault defects were detected in any of these constituents in either of the coatings. Since plastic deformation influences the stress state, this result is important. It is likely that the factors such as a different materials system (SiC/Al vs. TiC/Al), different amounts of reinforcement (10–20% vs. 60%), and different laser processing modes (pulse vs. continuous) have contributed to the difference in physical and structural changes occurring at sub-micron levels.

The interplanar spacing ($d_{\phi\psi}$) for a particular reflection is determined via Bragg's law, and the corresponding strain $\varepsilon_{\phi\psi}$ is calculated using Eq. (2) with stress-free interplanar spacing (d_0). After the strain values are calculated, the corresponding stress values for each reflection can then be obtained using the elastic modulus and Poisson's ratio for each corresponding phase. Since both Al and TiC single-crystals are nearly elastically isotropic [28], literature values of elastic modulus and Poisson's ratio were used (Table 1) [21,29,30]. The resulting stress components for each phase and their standard deviations are presented in Table 2. Since the two normal stresses (σ_{11}, σ_{22}), in the directions along the length of the laser track and transverse to the laser track, respectively, are the primary stresses of interest, further discussion in the paper is limited to only these stresses. In order to simplify the investigation and to achieve a better understanding about stress variation as a function of the processing speed, the following simplifications were adopted.

Stresses observed in all the phases were considered uniform throughout the X-ray penetration depth. This assumption is supported in part by detailed phase identification and calculations for the relative volume fraction of each phase which revealed a uniform distribution of phases throughout the thickness of the coating (Fig. 2) indicating an absence of compositional gradient along the depth of the coating [31]. The absence of a compositional gradient and negligible shear stresses through the X-ray penetration depth can be corroborated by the non-curved and non-parabolic nature, respectively, of the '$d_{\phi\psi}$ vs. $\sin^2\psi$' curves seen in Figs. 5a and 5b [32]. Although, trace amounts of free silicon were observed with XRD [31], the presence of these peaks was intermittent and often of low intensity. Consequently, a residual stress analysis was not done on silicon, and the coating was simplified to a two-phase coating.

Based on the above, and using Eqs. (6)–(11), the total stresses from Table 2 can be separated into their macro-stress and micro-stress components as presented in Figs. 7 and 8, respectively. Within the range of processing conditions explored in the present study, the average macro-stresses for both the alloys along the two principal directions (σ_{11} and σ_{22}) were observed to be compressive, unlike the tensile stresses described earlier [10,11]. Although the stresses developed owing to solidification during laser–material interactions are tensile, the contribution of compressive stresses owing to the thermal expansion mismatch between the coating (TiC + Al matrix) and the substrate (base Al alloy) to the total stress condition can be much larger. Here, the composite coating has

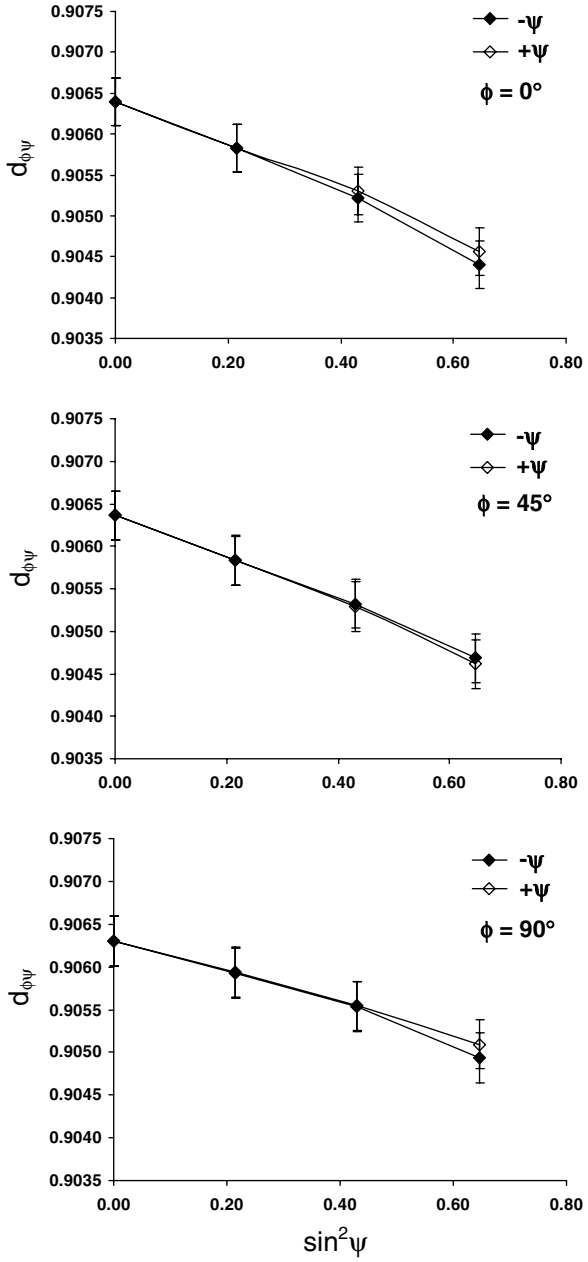

Fig. 5a. $\sin^2\psi$ plots for Al (420) reflection from TiC/Al coating on 2024 Al alloy substrate processed at 150 cm/min. The error bars represent the standard deviations.

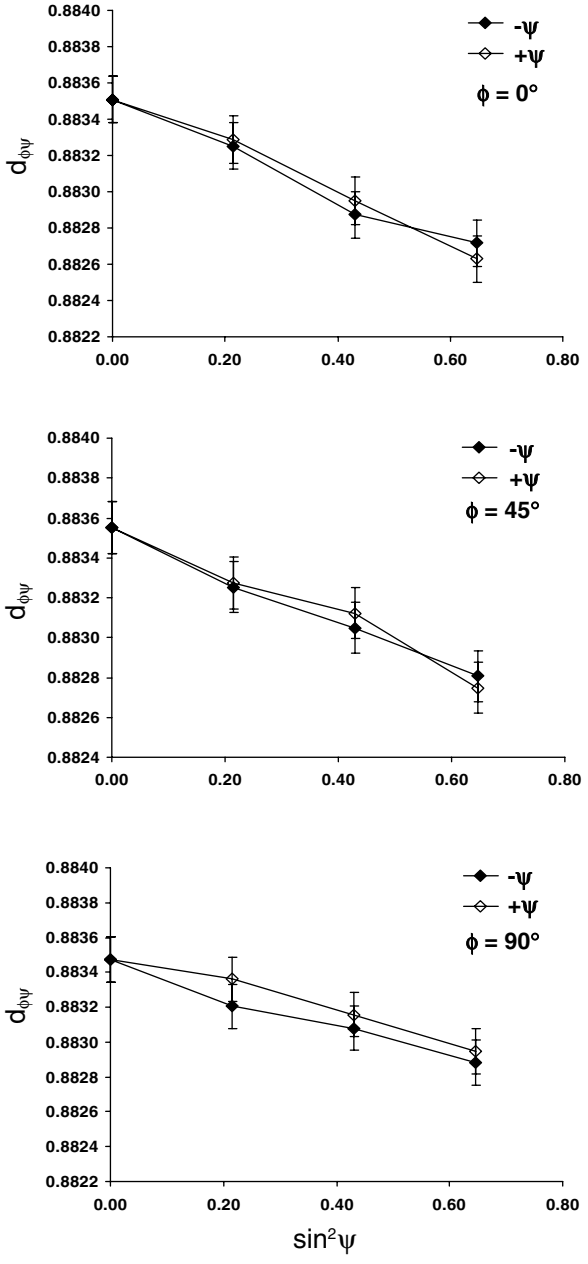

Fig. 5b. $\sin^2\psi$ plots for TiC (422) reflection from TiC/Al coating on 2024 Al alloy substrate processed at 150 cm/min. The error bars represent the standard deviations.

a thermal expansion coefficient of 13.6 μm/mK and Young's modulus 297 GPa (calculated using rule of mixtures). The composite thermal expansion coefficient is lower than that of either of the substrate materials (see Table 2). Therefore, the differential shrinkages of the coating with a large volume fraction of ceramic phase in metal matrix (60–65 vol.% TiC in Al-alloy) and the substrate (Al-alloys) during cooling from the processing temperature can give rise to compressive residual stresses [4]. Inserting the materials constants into Eq. (1) for a 0.1-mm-thick coating on a 6.9-mm-thick substrate yields a −1.7 GPa residual stress for a ΔT of 640 °C, providing an upper bound for comparison to the measured values.

Fig. 7 shows the variation in the magnitude of the macro-stress components (σ_{11}) and (σ_{22}), as a function of the laser traverse speed for 2024 and 6061 Al alloy substrates, respectively. From this figure, it is observed that as the laser traverse speed increased, the magnitudes of the stresses became less compressive, owing to increased debonding. This decrease can be explained on the basis of the different interaction times and material volumes associated with the varying processing speeds. As the traverse speed is increased, the amount of the laser-interacted material will decrease [31]. Based on this proposition, traversing the laser beam faster will increase the amount of compressive stresses developed in the coatings until

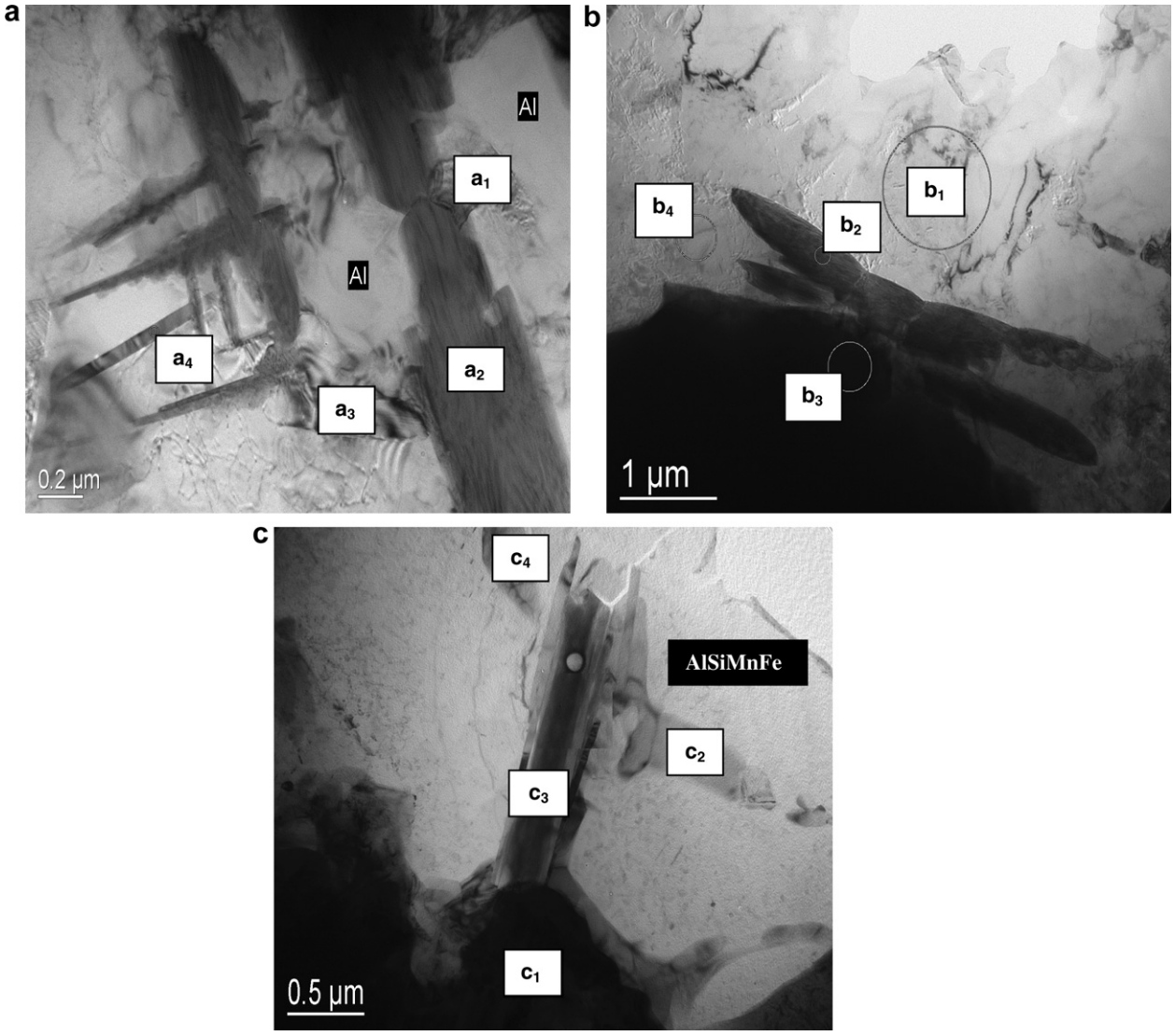

Fig. 6. TEM micrograph presenting an overview of the various phases in TiC/Al coating on (a) and (b) 6061 Al alloy substrate processed at 100 cm/min and (c) 2024 Al alloy substrate processed at 150 cm/min: a_1, Si; a_2, $TiSi_2$; a_3, Si; a_4, AlMgSiFe; b_1, Al–Si; b_2, $TiSi_2$; b_3, TiC; b_4, Al; c_1, TiC; c_2, Al_2Cu; c_3, Al_2O_3; and c_4, Al_2Cu.

Table 1
Mechanical and thermophysical properties of TiC, 2024 Al and 6061 Al [21,28–30,33]

Material	Elastic modulus (GPa)	Poisson's ratio	Thermal conductivity (W/mK)	Coefficient of thermal expansion (μm/mK)
TiC	450	0.2	27	7.2
2024 Al	72.4	0.3	120	23.8
6061 Al	68.9	0.3	154	23.6
SiC	400	0.18	120	4.85

debonding occurs (Fig. 3c, e and f). Higher stresses result in more debonding. Thus, post-laser processing measured lower residual stresses are directly related to the extent of debonding and only indirectly related to laser traverse speed. This result is also dependent upon the materials system under investigation. Once the coating has completely debonded, further increases in laser speed are not expected to have any influence on the residual stress.

The type of substrate material has also been observed to have a significant effect on the stress values. Fig. 7 indicates that 6061 Al alloy substrate samples processed at 150 cm/min are less compressive than the 2024 Al alloy substrate samples processed at the same speed. Since 6061 Al has a higher thermal conductivity (154 W/mK) than that of 2024 Al alloy (120 W/mK) [21], a thinner region (less volume of the material) is affected by the laser treatment,

Table 2
Total stress components for TiC/Al coating on 2024 Al and 6061 Al alloy substrate[a]

Substrate material	Laser traverse speed (cm/min)	Peaks	σ_{11} (MPa)	σ_{12} (MPa)	σ_{13} (MPa)	σ_{22} (MPa)	σ_{23} (MPa)	σ_{33} (MPa)
2024 Al	150	Al (420)	−189 (±43)	−11 (±17)	−4 (±12)	−130 (±30)	2 (±12)	−9 (±25)
		TiC (422)	−704 (±102)	−29 (±52)	−16 (±35)	−505 (±62)	20 (±35)	−143 (±44)
	175	Al (420)	−165 (±43)	−11 (±17)	2 (±12)	−140 (±30)	−3 (±12)	−12 (±25)
		TiC (422)	−589 (±102)	70 (±52)	10 (±35)	−640 (±62)	4 (±35)	−164 (±44)
	200	Al (420)	−123 (±43)	−17 (±17)	−18 (±12)	−60 (±30)	8 (±12)	−18 (±25)
		TiC (422)	−379 (±102)	63 (±52)	29 (±35)	−285 (±62)	−3 (±35)	−176 (±44)
6061 Al	100	Al (420)	−115 (±41)	2 (±16)	2 (±11)	−103 (±29)	−6 (±11)	−14 (±23)
		TiC (422)	−486 (±102)	25 (±52)	−4 (±35)	−374 (±62)	8 (±35)	−130 (±44)
	125	Al (420)	−38 (±41)	−5 (±16)	−12 (±11)	−39 (±29)	−2 (±11)	−1 (±23)
		TiC (422)	−197 (±102)	−9 (±52)	−13 (±35)	−214 (±62)	22 (±35)	−169 (±44)
	150	Al (420)	24 (±41)	−41 (±16)	−12 (±11)	−7 (±29)	−5 (±11)	41 (±23)
		TiC (422)	−279 (±102)	58 (±52)	−11 (±35)	−179 (±62)	12 (±35)	−150 (±44)

[a] Values in the parentheses are estimated standard deviations.

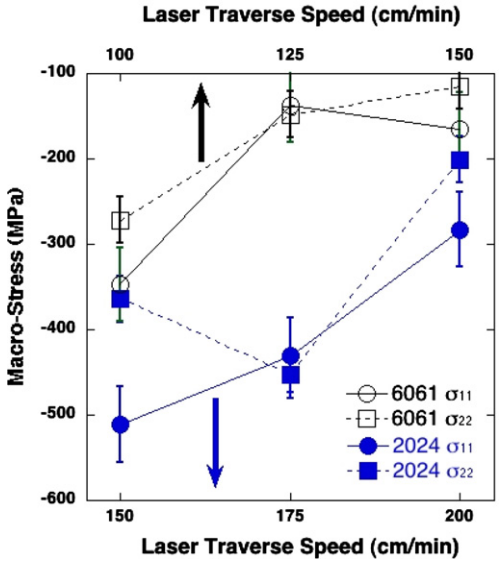

Fig. 7. Variation in the magnitude of macro-stress component σ_{11} and σ_{22} as a function of the laser traverse speed for TiC/Al coating on 2024 Al and 6061 Al alloy substrates. The error bars represent the standard deviations.

increasing the compressive stress contribution to the macro-stress prior to debonding initiation. As described above, as the traverse speed increases, the magnitude of post-laser process measured compressive stress in case of 6061 Al alloy decreases, reflecting the higher extent of partial debonding of the coating even at lower speeds (Fig. 3(e) for 6061 Al-alloy coating as compared with Fig. 3c for 2024 Al-alloy coating). For a similar extent of debonding, the residual macro-stresses are smaller in the 6061 alloy. This suggests that some additional stress relief occurred between the coating and substrate region, owing to the larger thermal conductivity.

Fig. 8 indicates that micro-stresses in the TiC particles (reinforcement) are compressive; whereas those in the Al phase (matrix) are tensile. Since no plastic deformation was observed in these coatings, the origin of micro-stresses appears to be best explained by the difference in the thermal expansion coefficient between TiC and Al. During the cooling process, the metal in the matrix shrinks more than the ceramic reinforcement, which creates very high compressive stresses in the reinforcement. Although no other

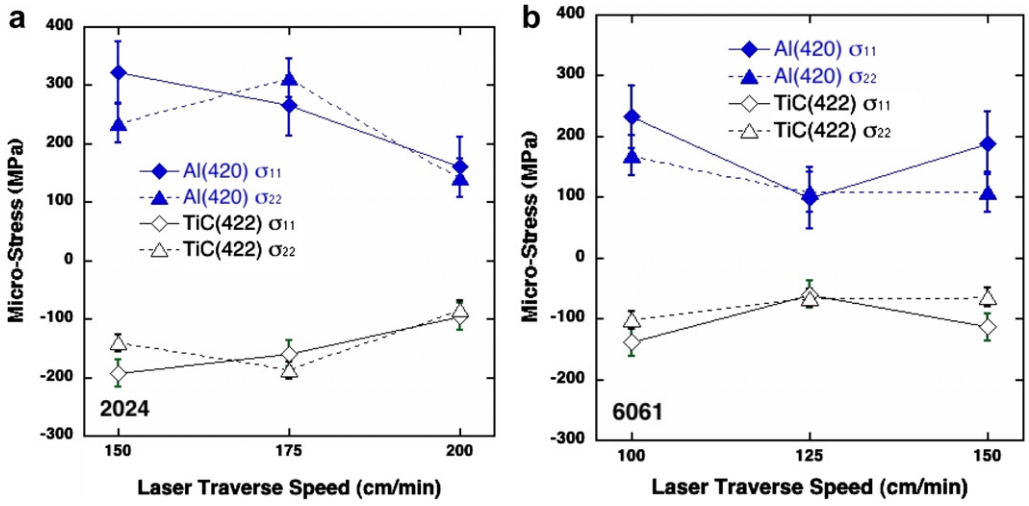

Fig. 8. Variation of micro-stresses within Al and TiC phases as a function of laser traverse speed for TiC/Al coating on (a) 2024 Al alloy substrate and (b) 6061 Al alloy substrate. The error bars represent the standard deviations.

residual micro-stress values as determined by diffraction methods for a TiC/Al system are available, values for a similar system, SiC/Al, can be compared with the measured values here. SiC has a Young's modulus, Poisson's ratio and coefficient of thermal expansion similar to that of TiC (see Table 1). Li and Londini [34] report measured values due to thermal expansion mismatch of −200 and 60 MPa in SiC whiskers (27 vol.%) and aluminum matrix, respectively, which are comparable with the micro-stress values measured in this study. Smith et al. [35] reported residual stresses of −299 and 71 MPa in SiC spheres (20 vol.%) and aluminum matrix. Arsenault and Taya [36] report micro-stresses of 400 and 231 MPa within the aluminum matrices of 5 and 20 vol.% SiC whisker/aluminum composites, respectively. Relative to these values, the micro-stresses for the aluminum in Fig. 8 were larger, possibly owing to the higher volume faction (60–65 vol.%) of reinforcing phase which would limit dislocation generation and motion, as suggested elsewhere [35].

From the above discussion, macro-stresses are largely influenced by the extent of debonding produced due to increased stresses with increased laser traverse speed. Conversely, the micro-stresses in the individual phases are relatively independent of the debonding/processing condition, as seen in Fig. 8a and b. Generally, the elastic incompability, temperature variations and thermal expansion mismatch are expected to be relatively constant at the micro-level. Further, the randomly oriented and uniformly distributed TiC particles, irrespective of processing conditions, support this as well.

5. Summary

X-ray residual stress measurements of laser-processed ceramic composite coatings on 2024 and 6061 Al alloy substrates were determined. The following is a summary of the observations:

(1) For all coatings and for the range of processing parameters employed, the residual macro-stresses were compressive in nature. The residual micro-stresses in the Al matrix of the coating were tensile, whereas those in the TiC particles were compressive.
(2) The magnitude of the post-laser-processing measured compressive residual macro-stresses was observed to decrease owing to increased debonding with increasing laser traverse speed. Changes in the magnitude of the macro-stresses were also observed with the change in the substrate material. The micro-stresses within the individual phases were independent of the processing conditions as well as the type of the Al-alloy material system.
(3) The $d_{\phi\psi}$ vs. $\sin^2\psi$ plots for matrix (Al) and reinforcement (TiC) showed linear trends, indicating the presence of only biaxial stresses and very small shear stresses.
(4) TEM characterization found no evidence of plastic deformation, which supports the residual stress data. The origin of the macro-stresses is thought to be dominated by the thermal expansion mismatch between the coating and the substrate.

Acknowledgments

The authors acknowledge the residual stress research sponsored by the Assistant Secretary for Energy Efficiency and Renewable Energy, Office of FreedomCAR and Vehicle Technologies, as part of the High Temperature Materials Laboratory User Program, Oak Ridge National Laboratory, managed by UT-Battelle, LLC, for the US Department of Energy under Contract Number DE-AC05-00OR22725.

References

[1] Katipelli LR, Agarwal A, Dahotre NB. Appl Surf Sci 2000;153(2):65.
[2] Dahotre NB, Shah S. Adv Eng Mater 2001;3(9):675.
[3] Dahotre NB, Nayak S, Popoola O. Jom 2001;53(9):44.
[4] Albert Sue J, Schajer GS. Stress determination for coatings. In: Lampman SR, Reidenbach F, editors. Surface engineering. ASM handbook, vol. 5. Materials Park (OH): ASM International; 1998. p. 647.
[5] Mura T. Micromechanics of defects in solids. 2nd ed. Boston: Kluwer Academic; 1982. p. 1.
[6] Noyan IC, Cohen JB. Residual stress: measurement by diffraction and interpretation. New York, NY: Springer; 1987. p. 47–51, 110, 125, and 129.
[7] Cohen JB. Powder Diffraction 1986;1(2):15.
[8] Majumdar JD, Manna I. Mater Sci Eng A 1999;268:216.
[9] De Hosson JThM, Van Otterloo DM, Noordhuis J. Microstructure and mechanical properties of laser treated aluminum alloys. In: Mazumder J, Conde O, Villar R, Steen W, editors. Proceedings of the NATO advanced study institute on laser processing: surface treatment and film deposition. Sesimbra, Portugal 1994. The Netherlands: Kluwer Academic; 1996. p. 511.
[10] James MR, Gnanamuthu DS, Moores R. J Scrip Metall 1984;18:357.
[11] Riabkina-Fishman M, Zevin LS, Zahavi J. J Mater Sci Lett 1988;7:741.
[12] Noordhuis J, De Hosson JThM. Acta Metall Mater 1992;40:3317.
[13] Noordhuis J, De Hosson JThM. Acta Metall Mater 1993;41:1989.
[14] Van Brussel BA, Hegge HJ, De Hosson JThM, Delhez R, De Keijser ThH, Van der Pers NM. Scrip Metall Mater 1991;25:779.
[15] Van Brussel BA, De Hosson JThM. Mater Sci Eng A 1993;161:83.
[16] Zhang S, Xie H, Zeng X, Hing P. Surf Coat Tech 1999;122:219.
[17] Lu J, Miege B, Flavenot JF, Thery S. J Comp Tech Res JCTRER 1990;12(4):232.
[18] Matejicek J, Sampath S, Dusky J. J Ther Spray Tech 1998;7(4):489.
[19] Abuhasan A, Balasingh C, Predecki P. J Am Ceram Soc 1990;73(8):2474.
[20] Dölle H, Hauk V. Z f Metalkde 1977;68:728.
[21] Properties of wrought aluminum alloys. In: Davis JR, editor. Aluminum and aluminum alloys, ASM specialty handbook. Materials Park (OH): ASM International; 1993. p. 653 and 686.
[22] Schuster M, Gobel H. Application of graded multilayer optics for X-ray diffraction. In: Gilfrich JV, Noyan IC, Jenkins R, Huang TC, Snyder RL, Smith DK, Zaitz MA, Predecki PK, editors. Advances in X-ray analysis, vol. 39. New York, NY: Plenum Press; 1995. p. 57.
[23] Watkins TR, Cavin OB, Bai J, Chediak JA. Residual stress measurements using parallel beam optics. In: Huang TC, Buhrke VE, Gilfrich JV, Havrilla GJ, Noyan IC, Snyder RL, editors.

Advances in X-ray analysis, vol. 46. Newton Square, PA: ICDD. p. 119. CD ROM.
[24] Cullity BD, Stock SR. Stress measurement. In: Horton MJ, Curless L, O'Brien, George DA, Disanno S, editors. Elements of X-ray diffraction. Englewood Cliffs (NJ): Prentice Hall; 1978. p. 453.
[25] Kadolkar PB. Appendix A. Master's thesis, Residual stress and cohesive strength of TiC composite coating on aluminum alloys during laser surface engineering. Knoxville, TN: The University of Tennessee; 2000. p. 109.
[26] Noyan IC, Cohen JB. Mater Sci Eng 1985;75:179.
[27] Dahotre NB, McCay MH, McCay TD, Gopinathan S, Allard LF. J Mater Res 1991;6(3):514.
[28] Chung DH, Buessem WR. The elastic anisotropy of crystals. In: Vahldiek FW, Mersol SA, editors. Anisotropy in single-crystal refractory compounds, vol. 2. New York, NY: Plenum Press; 1968. p. 217.
[29] Toth LE. General properties, preparation and characterization. In: Margrave JL, editor. Transition metal carbides and nitrides. New York, NY: Academic Press; 1971. p. 6.
[30] Bhushan B, Gupta BK. Handbook of tribology: materials, coatings and surface treatments. In: Hauserman R, editor. Metals and ceramics. New York (NY): McGraw Hill Inc; 1991. p. 4.53.
[31] Kadolkar PB, Dahotre NB. Appl Surf Sci 2002;199:222.
[32] Lu J, Retraint D. J Strain Anal 1998;33(2):127.
[33] Watkins TR, Green DJ. J Am Ceram Soc 1993;76(12):3066.
[34] Li A, Londini A. J Comp Mater 2002;37(7):873.
[35] Smith LF, Krawitz AD, Clarke P, Siamotoa S, Shi N, Arsenault RJ. Mater Sci Eng A 1992;159:L13.
[36] Arsenault RJ, Taya M. Acta Metall 1987;35(3):651.